Dalton Transactions

RSC Publishing

PAPER

Cluster-derived Ir–Sn/SiO_2 catalysts for the catalytic dehydrogenation of propane: a spectroscopic study†

Cite this: *Dalton Trans.*, 2013, **42**, 12714

A. Gallo,[a] R. Psaro,[b] M. Guidotti,*[b] V. Dal Santo,*[b] R. Della Pergola,[c] D. Masih[d] and Y. Izumi[e]

Received 2nd May 2013,
Accepted 14th May 2013

DOI: 10.1039/c3dt51144h

www.rsc.org/dalton

Ir–Sn bimetallic silica-based materials have been prepared *via* deposition of the molecular organometallic clusters $(NEt_4)_2[Ir_4(CO)_{10}(SnCl_3)_2]$ and $NEt_4[Ir_6(CO)_{15}(SnCl_3)]$ or *via* deposition of Sn organometallic precursor $Sn(n\text{-}C_4H_9)_4$ onto pre-formed Ir metal particles. These solids possess promising properties, in terms of selectivity, as catalysts for propane dehydrogenation to propene. Detailed CO-adsorption DRIFTS, XANES and EXAFS characterization studies have been performed on these systems in order to compare the structural and electronic evolution of systems in relation to the nature of the Ir–Sn bonds present in the precursor compounds and to propose a structural model of the Ir–Sn species present at the silica surface of the final catalyst.

1. Introduction

In recent years, the worldwide demand for propene has rapidly grown, as it plays a pivotal role as a feedstock for a large variety of polymers and of intermediates for the chemical industry. Typically, propene is obtained from steam cracking and fluid catalytic cracking of naphtha. Nevertheless, due to the increasing propene demand and unstable oil prices, there is a real interest in developing alternative routes to alkene production, in particular, from light alkanes that are frequently wasted in crude oil refining plants. Such a route can be as well a viable starting point to be combined with the exploitation of renewable building blocks.[1–3] Dehydrogenation of propane is thus a promising alternative and a couple of propane dehydrogenation processes (Oleflex, Catofin or FBD-4) have already been set up at the industrial level.[4]

With this aim, bimetallic catalysts have shown good performances for many important reactions, such as hydrogenation of alkynes and dienes in olefins feedstock,[5] selective hydrogenation of unsaturated aldehydes,[6] preferential oxidation of CO,[7] hydrogen production[8] and light alkane dehydrogenation.[9–13] However, as shown in earlier studies, it has been a difficult task to understand the rationale behind a promotion effect of an inert metal on the catalytic behavior of a noble one.[14] For example, a relevant decrease in hydrogenolysis properties of a Group 8, 9 or 10 metal occurs when a Group 14 metal is added as a promoter.[15–17] But the reason for such a decrease is still a matter of debate.

So far, this behavior has been principally ascribed to two different effects: the so-called *geometric* and *electronic* effects (*cf.* ref. 8 and references therein). The *geometric* effect is the result of the dilution of surface metal atoms by atoms of another metal (the promoter) and the surface ensembles of the main metal component are thus reduced in size. Such an effect is related to "structure sensitive" and "structure insensitive" reactions. In fact, some reactions, such as hydrogenolysis,[18,19] require a defined number of contiguous surface active metal atoms to proceed, whilst others, like dehydrogenation, do not. On the other hand, the *electronic* effect is related to a change in noble metal surface electronic density due to the presence of inert metal atoms and to the difference in electronic affinity between the main metal component and the promoter. As a consequence, a different interaction with the reacting molecules (adsorption/desorption of reagents/reaction intermediates/products) can occur and modify their catalytic properties. However, the discrimination between electronic and geometric effects has not yet been adequately understood for many catalytic systems. Together with these major structural and/or morphological effects, other important positive effects can arise from the addition of a metal promoter in these systems, such as improved coke resistance, enhanced thermal stability and increased resistance to poisoning.

Pt–Sn systems have been deeply studied by many authors because of their good catalytic performances in various reactions like reforming[20] and dehydrogenation,[21] in particular, of

[a]*Department of Chemical Engineering, University of California, Santa Barbara, CA 93106-5080, USA*
[b]*CNR-Istituto di Scienze e Tecnologie Molecolari, via Golgi 19, 20133 Milano, Italy. E-mail: m.guidotti@istm.cnr.it, v.dalsanto@istm.cnr.it*
[c]*Dipartimento di Scienze dell'ambiente e del territorio e di Scienze della Terra, Università di Milano-Bicocca, piazza della Scienza 1, 20126 Milano, Italy*
[d]*KAUST Catalysis Center, King Abdullah University of Science and Technology, Thuwal 23955-6900, Saudi Arabia*
[e]*Department of Chemistry, Graduate School of Science, Chiba University, Yayoi 1-33, Inage-ku, Chiba 263-8522, Japan*
†Dedicated to the memory of Dr Laura Sordelli.

propane[22] and isobutane.[23,24] Tin affects deeply Pt catalytic properties. In particular, Sn prevents Pt-catalyzed hydrogenolysis and also particles sintering and can reduce the rate of coke formation.[25–27] However, characterization studies contradict each other about the role of tin as a promoter. Some authors, on the basis of temperature programmed desorption (TPD) of adsorbed CO monitored by infrared spectroscopy and of calorimetric measurements of H_2 and CO adsorption,[21,25,28] observed a decrease in the number of surface contiguous Pt atoms due to the presence of tin that acts as a diluting component, thus attributing the Sn promotion mainly to the geometric effect. On the other hand, from XPS and H_2 or CO adsorption studies, a change in binding energy (BE) that is more consistent with the electronic effect was detected.[29] The lowering of the BE for platinum was, in fact, interpreted as an electron transfer from tin to platinum.

Another bimetallic system similar to Pt–Sn is the Ir–Sn one. Yet, characterization of them is still rare. Iridium is a noble metal exhibiting strong hydrogenolysis properties that can be deeply inhibited by the presence of Sn. In fact, Ir–Sn catalysts, supported on Na-Y zeolite or silica, showed good performances in propane dehydrogenation.[30] Moreover, this behavior depends basically on the synthesis method of catalysts and on the nature of the support. For silica-supported samples, only bimetallic cluster-derived catalysts showed propene selectivity up to 95%. In contrast, for Na–Y-supported samples, both bimetallic cluster-derived catalysts and monometallic precursor-derived ones were very selective for dehydrogenation.

Some years ago, some of us showed excellent performances of bimetallic catalysts obtained from Ir–Sn carbonyl cluster precursors or prepared by deposition of an organometallic Sn precursor onto pre-formed Ir nanoparticles in the gas-phase dehydrogenation of propane at 773 K.[31] In particular, an optimal selectivity to propene and a high catalyst stability were recorded. In order to study the generation and structural features of bimetallic supported Ir–Sn nanoparticles, we deposited two clusters with pre-formed Ir–Sn bonds onto ordered high surface area silica supports. In this work, we show the results of the characterization of such bimetallic cluster-derived and monometallic precursor-derived silica supported Ir–Sn catalysts. We studied both iridium and tin sites by means of DRIFTS-monitored CO chemisorption, as well as of Ir L_3-edge and Sn K-edge X-ray absorption spectroscopy (XAS) in order to understand the promotion effect of tin. Indeed, the aim is to understand how tin affects iridium. The correlation of the results of previous catalytic tests with characterization studies will allow us to better understand the chemical surrounding of the active metal sites on the support.

2. Experimental

2.1. Catalysts preparation

Two mesoporous silica materials were used as supports: a commercially available non-ordered silica purchased from Grace Davison (denoted as SiO_2; mean pore diameter 20.4 nm, total pore volume 1.48 $cm^3\ g^{-1}$ and specific surface area 290 $m^2\ g^{-1}$) and an ordered purely siliceous MCM-41 (mean pore diameter 2.8 nm, total pore volume 1.36 $cm^3\ g^{-1}$ and specific surface area 1024 $m^2\ g^{-1}$). SiO_2 was stirred for 5 h in 1 M HNO_3 and then washed before use with ultrapure deionised water (MilliQ; 18 MΩ cm^{-1}) until neutrality was reached. MCM-41 was synthesized with a pore wall thickness of about 2 nm according to the procedure described in the literature.[32]

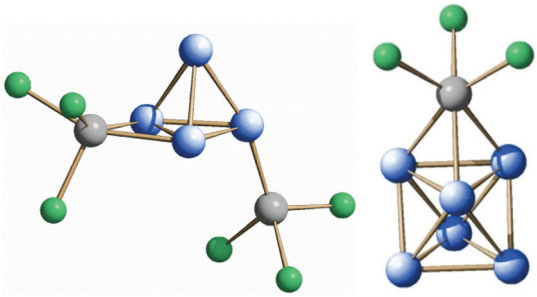

Scheme 1 The solid state structures of the clusters $[Ir_4(CO)_{10}(SnCl_3)(\mu\text{-}SnCl_3)]^{2-}$ and $[Ir_6(CO)_{15}(\mu_3\text{-}SnCl_3)]^{-}$. Blue: iridium; light grey: tin; green: chlorine (carbonyl omitted).

Two main synthetic ways were followed to obtain the catalysts: a "single source" method and a "dual source" one.

Single source precursors were $(NEt_4)_2[Ir_4(CO)_{10}(SnCl_3)_2]$ and $NEt_4[Ir_6(CO)_{15}(SnCl_3)]$ organometallic clusters, prepared as described elsewhere[33] (Scheme 1).

Before impregnation, the non-ordered silica was treated at 773 K in air for 5 h and *in vacuo* overnight, stirred in MilliQ water for 4 h, dried and then treated at 573 K in air for 5 h and *in vacuo* overnight. Similarly, MCM-41 was treated at 573 K in air and then left *in vacuo* overnight. Impregnation occurred *via* an anhydrous CH_2Cl_2 (Fluka) solution of the cluster precursor. The suspension was stirred for 12 h under Ar. The solvent was then removed under vacuum in the case of SiO_2, whereas by filtration for MCM-41.

Monometallic and *dual source* bimetallic catalysts were also synthesised using monometallic precursors. First, monometallic Ir samples were prepared by impregnating the supports with a solution of $IrCl_3{\cdot}3H_2O$ (Engelhardt) in a hydrochloric acid aqueous solution (typically 1.5 mL of 36% HCl in 60 mL of MilliQ water). After drying, the iridium-containing samples were calcined for 1 h under oxygen flow (100 mL min^{-1}; 573 K) and then reduced for 1 h under hydrogen flow (100 mL min^{-1}; 643 K). Then, bimetallic samples were synthesised by evaporation of a solution of $Sn(n\text{-}C_4H_9)_4$ (Aldrich, 93%) in anhydrous toluene (Riedel de Haen).

All operations were conducted under Ar inert atmosphere, unless otherwise specified, and all catalysts were stored under Ar atmosphere prior to use. The metal contents of the prepared catalysts, and the nature of the precursors they are obtained from, are summarised in Table 1.

In summary, $Ir_{5.9}$ + Sn/SiO_2 and $Ir_{1.8}$ + Sn/SiO_2 were obtained *via* the dual source method, whereas $[Ir_4Sn_2]/SiO_2$, $[Ir_4Sn_2]$/MCM-41 and $[Ir_6Sn]$/MCM-41 *via* the single source one.

Table 1 Catalysts composition and metal particle dispersion

Catalyst	Precursor	Ir content[a] (wt%)	Sn content[a] (wt%)	N_S/N_T[b] (%)
Ir/SiO_2	$IrCl_3$	0.86	—	58
$Ir_{5.9}$ + Sn/SiO_2	$IrCl_3$ + Sn(*n*-Bu)$_4$	0.78	0.08	54
$Ir_{1.8}$ + Sn/SiO_2	$IrCl_3$ + Sn(*n*-Bu)$_4$	0.78	0.27	65
Ir/MCM-41	$IrCl_3$	1.28	—	70
$[Ir_4Sn_2]/SiO_2$	$(NEt_4)_2[Ir_4(CO)_{10}(SnCl_3)_2]$	1.02	0.29	70
$[Ir_4Sn_2]$/MCM-41	$(NEt_4)_2[Ir_4(CO)_{10}(SnCl_3)_2]$	0.68	0.22	73
$[Ir_6Sn]$/MCM-41	$(NEt_4)[Ir_6(CO)_{15}(SnCl_3)]$	0.71	0.11	71

[a] As obtained from the ICP-AES analysis. [b] Dispersions calculated as the surface atoms to total atoms ratio from average diameters based on HR-TEM observations assuming Ir fcc packing in a truncated cubo-octahedron geometry for reduced samples only.

2.2. DRIFT characterization

IR spectra were collected fusing a home-made DRIFTS cell, which allows *in situ* treatment of the samples,[34] inserted in the beam path of a DigilabFTS-60A spectrometer. The catalysts were loaded under inert atmosphere in the reaction chamber. Helium was fluxed for a few minutes (at the rate of 25 mL min^{-1}). After He purging, H_2 was admitted (25 mL min^{-1}) at room temperature for 15 min. Activation conditions were similar to the ones of catalytic tests:[31] the catalysts were heated to 773 K under hydrogen (25 ml min^{-1}) at the ramping rate of 10 K min^{-1} for 1 h. After cooling down to room temperature in flowing He (25 mL min^{-1}), CO was fluxed in the cell (25 mL min^{-1}). When the adsorption band intensity reached constant values, He was introduced to remove gaseous and weakly bound CO.

2.3. EXAFS–XANES spectroscopy

EXAFS (extended X-ray absorption fine structure) and XANES (X-ray absorption near edge spectroscopy) measurements at the Ir L_3-edge and Sn K-edge have been performed on the following samples: (a) pure cluster complexes $(NEt_4)_2[Ir_4(CO)_{10}(SnCl_3)_2]$ and $(NEt_4)[Ir_6(CO)_{15}(SnCl_3)]$; (b) silica supported $(NEt_4)_2[Ir_4(CO)_{10}(SnCl_3)_2]$ and $(NEt_4)[Ir_6CO)_{15}(SnCl_3)]$ samples after reduction (Table 1), respectively, denoted as $[Ir_4Sn_2]/SiO_2$, $[Ir_4Sn_2]$/MCM-41 and $[Ir_6Sn]$/MCM-41; (c) samples (b) at the end of a catalytic run; (d) the dual step sample $Ir_{1.8}$ + Sn/SiO_2 after reduction; and (e) previous samples, as in (d), at the end of a catalytic run.

The experiments on samples at point (a) have been carried out at the Sn K-edge and Ir L_3-edge at the SAMBA beamline of the SOLEIL synchrotron in Saclay (Paris, France), using a double-crystal Si(220) monochromator (resolution of 1.6 eV at the Sn edge and 0.6 eV at the Ir edge) from the ring operated at 2.75 GeV, and at the KEK-PF-AR synchrotron facility at the beamline NW10A (Tsukuba, Japan) using a double-crystal Si(311) monochromator from the ring operated at 6.5 GeV, respectively.

The spectra have been recorded in transmission mode on samples sealed inside sample-holders loaded under argon atmosphere and measured at room temperature over a range of 1000 eV above the edge, with a scanning step of 0.05 eV and 2–4 seconds integration per point. Each spectrum measurement has been repeated three or four times for the signal-to-noise ratio optimization and for the error bars evaluation.

The Ir L_3-edge experiments on samples from points (b) to (e) have been carried out at the XAFS beamline of the Elettra synchrotron in Trieste (Italy), with a double-crystal Si(311) monochromator and the ring operated at 2.0 GeV. The spectra have been recorded in transmission mode on samples sealed inside sample-holders loaded under a nitrogen atmosphere and measured at room temperature over a range of 1000 eV above the edge, with a sampling step of 2 eV and 2–4 seconds integration per data point. Each spectrum measurement was repeated three or four times for the signal-to-noise ratio optimization and for the error bars evaluation.

Data analysis has been performed with the FEFF8 software package.[35] Experimental EXAFS $\chi(k)$ functions have been extracted from the absorption spectra with a standard procedure and Fourier transformed over a *k*-range of 25–130 nm^{-1}. The main peaks of the Fourier transformed modulus have been filtered and analyzed with a nonlinear least-squares fit program which provides the atomic species, the coordination number (N) of nearest neighbours, their distance R from the absorber atom and the disorder σ_{DW} factor for each shell.

Sn K-edge XANES spectra on a part of the samples at points (a)–(e) were measured at 290 K on beamline 10B at KEK in fluorescence detection mode using a Lytle detector. Sn-edge EXAFS data on a part of the samples at points (a)–(e) were obtained in transmission mode at KEK-PF-AR. The curve fit parameters were derived from EXAFS spectra for SnO powder and $(NEt_4)_2[Ir_4(CO)_{10}(SnCl_3)_2]$ for Sn–O, Sn–Cl, and Sn–Ir bonds, respectively. As references standards for the evaluation, theoretical phase and amplitude functions generated from FEFF8.2[35] for Sn–O, Sn–Cl, Sn–Sn, Ir–O and Ir–Ir bonds, the EXAFS spectra of SnO, $SnCl_2$ and Sn foil, IrO_2 and Ir foil, respectively, have been also employed. The curve fit parameters are first evaluated from the interatomic distances and the coordination number in crystal data of pure clusters $[Ir_4(CO)_{12}]$,[36] $[Ir_6(CO)_{16}]$,[37] $(NEt_4)_2[Ir_4(CO)_{10}(SnCl_3)_2]$ and $(NEt_4)[Ir_6(CO)_{15}(SnCl_3)]$.[38]

3. Results

3.1. DRIFT characterization

Carbon monoxide is a suitable probe to investigate the chemical nature and the electronic properties of Ir species. Since at room temperature CO chemisorbs only on Ir sites, it can be used as a selective probe also in the presence of Sn. As a common behaviour to all samples, CO stretching bands were detected only above 1900 cm^{-1}, indicating the absence of bridged CO species.[39] In particular, after CO exposure one IR

band appeared in the region between 1900 and 2100 cm^{-1}. Such evidence, reported also by other authors, is consistent with the presence of CO linearly chemisorbed on dispersed Ir metallic particles.[40]

The attribution of IR absorption bands due to CO adsorbed on Ir sites is not a trivial task, since a commonly accepted interpretation is lacking in the available literature. The particle-size effect was studied by many authors and they generally agree that an increase in particles size leads to IR bands at higher frequency.[41] However, the same authors have studied low and highly dispersed Ir particles on alumina and they have assigned the two bands located at 2050 and at 2075 cm^{-1} respectively to CO adsorbed on coordinatively-unsaturated (at edges, corners, *etc.*) sites and on coordinatively-saturated (on planes) sites.

Alternative assignments of high, medium and low frequency bands were proposed by Solymosi *et al.*[42] Three IR CO absorption bands were reported on reduced 5% Ir/Al_2O_3 catalysts located respectively at 2102, 2081 and 2040 cm^{-1}. The 2012 and 2040 cm^{-1} frequency bands were attributed to symmetric and antisymmetric stretchings of Ir dicarbonyl species, while the one of 2081 cm^{-1} was attributed to CO linearly bonded to Ir clusters. Notably on silica supported 1% Ir sample, the authors found only one band located at 2070 cm^{-1}.

Comparable results were found by Tanaka *et al.* in alumina- and silica-supported $Ir_4(CO)_{12}$ catalysts.[43] The presence of tin in bimetallic Ir–Sn catalysts caused a different IR adsorption pattern and a general decrease in intensity was observed. For all bimetallic samples, obtained *via* either the single or dual source approach, the low wavenumber components of the adsorption bands increased in the IR pattern.

An alternative attribution of IR bands was proposed by McVicker *et al.*[44] The high frequency band (2060 cm^{-1}) was attributed to $Ir(CO)_2$-dicarbonyl species with two non-equivalent CO, thus showing only one CO stretching, the low frequency band (located at 2020 cm^{-1}) was attributed to Ir(CO)-monocarbonyl species. Since smaller particles present a higher fraction of edge and corner atoms able to chemisorb up to two CO per Ir atom, whereas Ir atoms in larger particles can chemisorb only one CO per metal atom, high frequency bands were attributed to highly dispersed Ir catalysts, and the low frequency one to samples with lower dispersion. A similar band located at 2070 cm^{-1} was observed by Erdöhely *et al.* for highly dispersed Ir on silica, magnesia and titania.[40]

Our results were in good agreement with those of McVicker and Erdöhely. The most dispersed samples are the ones supported over high-specific surface area MCM-41, showing linear adsorbed CO absorption falling at higher wavenumbers with respect to non-ordered SiO_2 supported catalysts that, in turn, show bands located at lower wavenumbers. A strong dependence of band position on metal dispersion was found for monometallic Ir catalysts supported on silica materials (namely Ir/SiO_2 and Ir/MCM-41) (Fig. 1a,b). Highly dispersed metallic particles caused a blue shift of CO IR absorption bands. In detail, in highly dispersed Ir/MCM-41 samples an

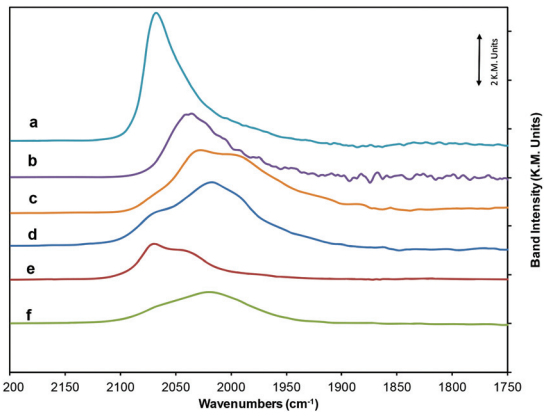

Fig. 1 DRIFT spectra for CO absorption on (a) Ir/MCM-41; (b) Ir/SiO_2; (c) $Ir_{1.8}$ + Sn/SiO_2; (d) $[Ir_4Sn_2]$/MCM-41; (e) $[Ir_6Sn_1]$/MCM-41; (f) $[Ir_4Sn_2]/SiO_2$.

asymmetric CO chemisorption band at *ca.* 2070 cm^{-1} was detected (Fig. 1a), whereas a decrease in intensity and a red shift to 2040 cm^{-1} occurred for less dispersed Ir/SiO_2 samples (Fig. 1b). The asymmetric adsorption revealed two main components: the main one located at 2039 cm^{-1} and a weak shoulder at 2003 cm^{-1} (a very weak shoulder at about 2070 cm^{-1} is also present). After deposition of Sn and activation, the IR pattern in the carbonyl region changed further (Fig. 1c). The presence of Sn, from $Sn(n\text{-}Bu)_4$, mainly affected the relative intensity of the component of the CO linearly adsorbed on the nanoparticles at 2039 cm^{-1}. In particular, for the sample $Ir_{1.8}$ + Sn/SiO_2 the band intensity at 2039 cm^{-1} decreased. Then, the peak maximum shifted to 2030 cm^{-1} and the shoulders at 2005 cm^{-1} and at 2070 cm^{-1} became more evident.

MCM-41 supported samples revealed similar features with a different relative intensity. Monometallic Ir catalyst showed a broad band with a maximum at 2067 cm^{-1}, typical of highly dispersed metallic particles; two shoulders located respectively at 2034 and 2000 cm^{-1} were also observed.

In conclusion, for dual source samples three bands ascribable to adsorbed CO were revealed. As a general consideration the relative intensity between these bands is strongly influenced by two main factors: the particles dimension for monometallic Ir samples and the presence of Sn for bimetallic ones. The addition of tin decreased the overall CO chemisorption, but influenced strongly the adsorption band at higher wavenumbers (2070 and 2030 cm^{-1}); thus, the relative intensity of the band at 2000 cm^{-1} was higher for bimetallic catalysts than the monometallic ones.

Single source catalysts showed some differences in IR absorption patterns, when compared with dual source derived samples (Fig. 1d–f). In fact, $[Ir_4Sn_2]$/MCM-41 revealed a CO adsorption band with a maximum at 2020 cm^{-1} and two shoulders, one located at 2070 cm^{-1} and a more relevant one at 2000 cm^{-1}. In the same way, the non-ordered silica supported cluster, $[Ir_4Sn_2]/SiO_2$, showed the same band after activation, but with a lower contribution of the two shoulders. In contrast, three similar components were detected for $[Ir_6Sn_1]$/

MCM-41, although their relative intensity was completely different (Fig. 1e). Indeed, also for this sample the band maximum was centred on the middle wavenumbers position, but with a more relevant contribution of a shoulder at higher wavenumbers. In conclusion, we found a general shift of the absorption band maxima towards lower wavenumbers when we compare cluster-derived samples to dual source-derived ones. This suggests a better interaction between Ir and Sn when a bimetallic precursor is used for the synthesis. In addition, the relative intensity of lower components was more relevant.

In order to study the samples surface stability under reaction conditions, CO chemisorption studies were also performed on the Ir/MCM-41 and $[Ir_4Sn_2]$/MCM-41 systems after a reaction time of 24 h. Before chemisorption experiments the samples were treated again under H_2 at 773 K for 1 h. During such a treatment no CH_4 evolution was detected by means of on-line QMS analysis on the outlet stream. Nevertheless, some coke residues were detected on the catalysts after 24 h on stream (1.06 and 2.42 wt% in carbon content for Ir/MCM-41 and $[Ir_4Sn_2]$/MCM-41, respectively, as from elemental C, H, N analysis). It is thus likely that these carbonaceous deposits, which are stable under such conditions, are graphitic in nature (the so-called "hard coke").[45]

After catalysis, Ir/MCM-41 samples showed a decrease in IR absorption and a shift of absorption maximum of the chemisorbed CO band to 2050 cm^{-1}. As a result of the reaction, the higher component at 2070 cm^{-1} was not present any more. Also the IR pattern for $[Ir_4Sn_2]$/MCM-41 changed after catalysis (Fig. 2). The intensity ratio of the 2020 to 1995 cm^{-1} band was reverted, now the 1995 cm^{-1} band being more intense. Thus, as a general behaviour, after catalysis there was a shift of the CO adsorption bands towards lower wavenumbers. Furthermore, this shift was more evident for the monometallic Ir sample than for the cluster-derived bimetallic one.

3.2. XANES

The Ir L_3-edge XANES analysis (Fig. 3) evidenced that the two pure clusters $(NEt_4)_2[Ir_4(CO)_{10}(SnCl_3)_2]$ and $NEt_4[Ir_6(CO)_{15}(SnCl_3)]$,

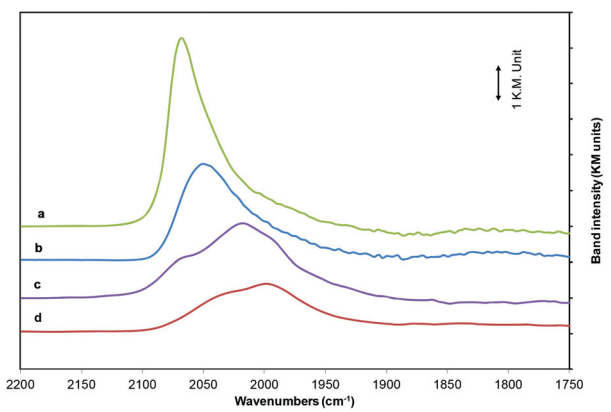

Fig. 2 DRIFT spectra for CO absorption on (a) Ir/MCM-41 before catalysis; (b) Ir/MCM-41 after 24 h catalysis; (c) Ir_4Sn_2/MCM-4 before catalysis; (d) Ir_4Sn_2/MCM-41 after 24 h catalysis.

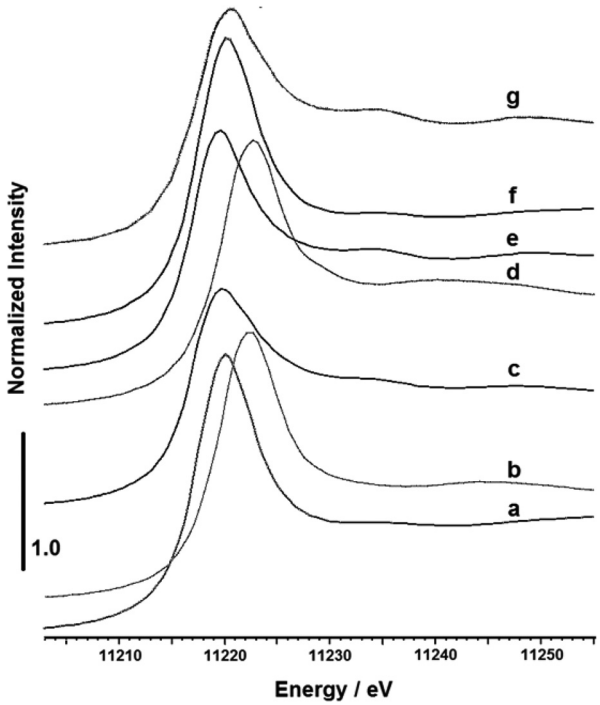

Fig. 3 Ir L_3-edge XANES spectra for Ir metal (g), Ir/SiO_2 (f), $Ir_{1.8}$ + Sn/SiO_2 (e), $(NEt_4)_2[Ir_4(CO)_{10}(SnCl_3)_2]$ (d), $[Ir_4Sn_2]/SiO_2$ (c), $NEt_4[Ir_6(CO)_{15}(SnCl_3)]$ (b), and $[Ir_6Sn]$/MCM-41 (a).

exhibit an Ir edge energy position and white line structure corresponding to the Ir^0 state due to the predominant metal–metal contribution from the core of the metal clusters (Scheme 1). This trend is also in agreement with the CO IR band position which corresponds to those of the complex $[Ir_4(CO)_{12}]^0$,[46] while an absorption edge shift of 2 eV towards lower energy with respect to the reference metal foil was observed in the data for all impregnated-reduced catalyst systems, demonstrating an average electron-rich character of Ir interacting with the support and/or the Sn atoms in contact with the catalyst metal particles. Any electron density variation on Ir among the different catalyst systems, due to particle size effect or interaction with the Sn, was below the energy resolution attained, under these conditions, in the spectra at the Ir L_3 edge.

The XANES analysis at the tin K-edge showed the following results: in the pure bimetallic cluster $(NEt_4)_2[Ir_4(CO)_{10}(SnCl_3)_2]$ dispersed in boron nitride (BN), the energy values of the Sn absorption edge and the white line peak top were close to those for the SnO reference compound (Fig. 4b,d), so the Sn species was essentially maintaining the native divalent state. Due to different coordination environments for the bimetallic cluster, the post-edge peak features were diminished, and the white line peak top intensity to post-edge depth ratio was low as compared to SnO. The catalyst prepared from bimetallic cluster $NEt_4[Ir_6(CO)_{10}(SnCl_3)]$ impregnation and following reduction in H_2 at 773 K exhibited higher edge energy, close to the Sn^{4+} state (Fig. 4c,g). The $[Ir_4Sn_2]/SiO_2$ catalyst prepared from the bimetallic $[NEt_4]_2[Ir_4(CO)_{10}(SnCl_3)_2]$ cluster after

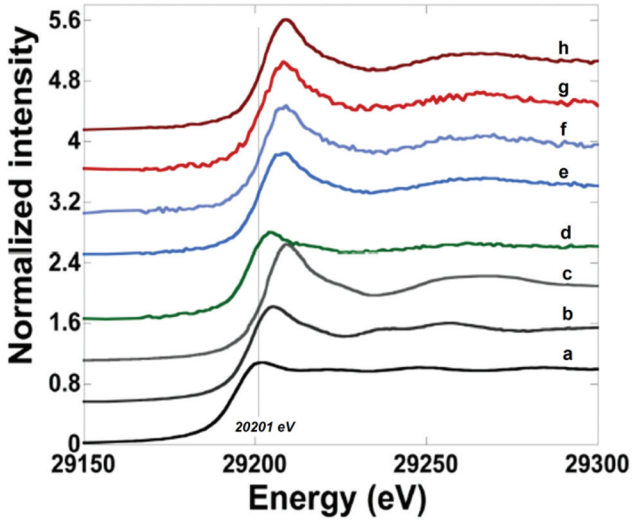

Fig. 4 Sn K-edge XANES spectra for Sn metal (a), $Sn^{II}O$ (b), $Sn^{IV}O_2$ (c), $(NEt_4)_2[Ir_4(CO)_{10}(SnCl_3)_2]$ (d), $Ir_{1.8}$ + Sn/SiO_2 (e), $Ir_{5.9}$ + Sn/SiO_2 (f), $[Ir_6Sn]$/MCM-41 (g), and $[Ir_4Sn_2]/SiO_2$ (h).

treatment at 773 K in H_2 also showed a tetravalent state of Sn species even though starting Sn was divalent (Fig. 4c,h). Conversely, the reduction of the samples synthesized by deposition of $Sn(n\text{-}Bu)_4$ led to a Sn edge position comparable to that of SnO_2. In the latter case the Sn absorption edge and white line peak top energy values were the highest for the catalyst with the lowest Sn contents (Ir/Sn = 6) (Fig. 4e,f). Such a behaviour can be correlated to the EXAFS edge shift, due to the diminution in electronic density (see section 3.3). Also the white line peak top to post-edge depth ratio decreased with an increase of Sn amount loaded in the catalysts (Ir/Sn = 2).

The spectra (e) and (f) for Ir_x + Sn/SiO_2 samples (Fig. 4) were basically similar to the one for SnO_2, but at a closer look, a weak shoulder feature was present in such spectra at 29 201 eV that was absent in spectrum (c) for SnO_2 (Fig. 4; reference line position). This shoulder feature suggests also the presence of metallic Sn sites in Ir nanoparticles in addition to tetravalent Sn sites.

In summary, Sn K-edge XANES patterns for the Ir–Sn species supported on SiO_2 and MCM-41 after reduction were similar to SnO_2, but the white line peak top to post-edge depth ratio was the highest for $[Ir_4Sn_2]/SiO_2$.

In particular, the trend in Fig. 4 for the Ir_x + Sn/SiO_2 samples evidences how the absorption edge progressively shifts towards the lower energy side, as the Sn amount in the catalyst increases. This trend implies that Sn acts as an effective electron donor to Ir and the donation extent per Sn atom is greater as the Sn amount becomes relatively smaller. In fact, the higher the total Sn amount, the higher is the overall electron-rich character of Ir. Moreover, the oxidation state for Sn of (IV) is reached when the Ir/Sn ratio is 6 (Fig. 4c, f). The XANES spectra for $[Ir_4Sn_2]$/MCM-41 and $[Ir_6Sn]$/MCM-41 are basically similar to those for Ir + Sn/SiO_2 (Ir/Sn = 2 and 6), respectively (spectra not shown). The extent of edge energy shift is slightly smaller (0.2–0.3 eV) for the supported bimetallic cluster on MCM-41 compared for that for Ir_x + Sn/SiO_2. This may be due to the difference of average metal particle size: 1.5 nm for supported bimetallic cluster samples and 1.9 nm for Ir_x + Sn/SiO_2 samples.

3.3. EXAFS

The fit results for the Ir L_3-edge of $[Ir_4Sn_2]$ and $[Ir_6Sn]$ on MCM-41 samples showed (Fig. 5 and Table 4) the formation of very small metal particles with a coordination number for the Ir–Ir scattering path of 3.4 and 3.1, respectively. Namely, for the Ir–Ir shell, an N of 4 corresponds to 0.8–0.9 nm average diameter of the Ir particle. A strong interaction with surface oxygen atoms was evidenced by the short distance Ir–O scattering path resulting from the fit. The metal dispersion of the two cluster-derived catalysts over MCM-41 is higher than that in any other reduced sample (see Table 4), in agreement with the average metal particle sizes detected by HR-TEM. Notably, even with a molar ratio of Ir/Sn of 1.8, no Ir–Sn scattering path was detected. This suggests a partial segregation of Sn species at the interface between the Ir nanoparticle and the silica support.

After reduction the structural evolution of the two cluster-derived catalysts was dramatically different on non-ordered silica and on MCM-41. In fact, on silica, larger metal particles were produced (an N_{Ir-Ir} of 6.5 corresponding to 1.4 nm average diameter) with respect to the 0.9 nm average particle size on MCM-41, with a parallel decrease of the support surface interaction contribution. The reduction of the silica-supported system obtained *via* the dual source indeed produces larger particles (Table 4). It is however worth mentioning that the catalytic properties of these samples are comparable. This excludes, therefore, a primary effect on the dehydrogenation activity of the dispersion or a relevant interaction with the support oxygen of the metal particles.

The Sn K-edge data of $[Ir_4Sn_2]$/MCM-41 and $[Ir_4Sn_2]/SiO_2$ catalysts suggest the coexistence of Sn interacting with oxygen

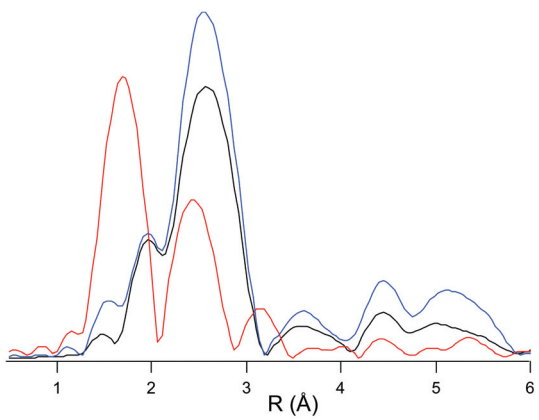

Fig. 5 Fourier transform of the Ir L_3-edge EXAFS spectra (phase shift uncorrected) of $[Ir_4Sn_2]$/MCM-41 (red), $[Ir_4Sn_2]/SiO_2$ (black) and $Ir_{1.8}$ + Sn/SiO_2 (blue) samples.

Table 2 EXAFS data fit at the Sn K-edge for pure compounds and silica-supported catalysts

	Shell Sn–O	Shell Sn–O	Shell Sn–Cl	Shell Sn–Ir and Sn–Sn	Shell Sn–Ir and Sn–Sn
$(NEt_4)_2[Ir_4(CO)_{10}(SnCl_3)_2]$	—	—	N = 3 σ = 0.056 R = 2.426	N = 2 σ = 0.05 R = 2.584	N = 1 σ = 0.05 R = 2.718
$[Ir_4Sn_2]$/MCM-41	N = 4.6 σ = 0.063 R = 2.040 ΔE = 4.4	—	—	—	N = 4.6 σ = 0.089 R = 2.865 ΔE = −21.1
$[Ir_4Sn_2]/SiO_2$	N = 3.3 σ = 0.063 R = 2.037 ΔE = 1.2	—	—	N = 0.8 σ = 0.069 R = 2.502 ΔE = 6.6	N = 1.2 σ = 0.069 R = 2.830 ΔE = −33.6
$Ir_{1.8}$ + Sn/SiO_2	N = 2.0 σ = 0.075 R = 1.997 ΔE = −21.5	N = 4.5 σ = 0.050 R = 2.106 ΔE = −1.0	—	—	N = 0.6 σ = 0.035 R = 2.887 ΔE = −41.3

The distance is expressed in angstroms, the DW factor in angstroms, and the energy shift in eV.

Table 3 EXAFS data fit at the Ir L_3-edge for pure compounds

	Shell Ir–C	Shell Ir–Sn	Shell Ir–Sn_2	Shell Ir–Ir	Shell Ir–Ir	Shell Ir–O
$Ir_4(CO)_{12}$	N = 3 σ = 0.085 R = 1.86 ΔE = 11.8	—	—	N = 3 σ = 0.019 R = 2.67 ΔE = 0	—	N = 3 σ = 0.079 R = 3.24 ΔE = 0
$Ir_6(CO)_{16}$	N = 2 σ = 0.085 R = 1.86 ΔE = 11.8	—	—	N = 4 σ = 0.07 R = 2.77 ΔE = 0	—	N = 2 σ = 0.079 R = 3.05 ΔE = 0
$(NEt_4)_2[Ir_4(CO)_{10}(SnCl_3)_2]$	N = 2.5 σ = 0.085 R = 1.86 ΔE = 11.8	N = 1.5 σ = 0.079 R = 2.580 ΔE = 8.9	— — — —	N = 1.5 σ = 0.019 R = 2.67 ΔE = 0	N = 1.5 σ = 0.009 R = 2.80 ΔE = 0	N = 2 σ = 0.079 R = 3.24 ΔE = 0

The distance is expressed in angstroms, the DW factor in angstroms, and the energy shift in eV.

and metallic Sn–Ir alloy (Fig. 6), as evidenced by an Sn–O scattering path at around 0.2 nm and two Sn–Ir ones at 0.25 nm, detected only for the SiO_2 supported catalyst, and at 0.28 nm. Due to the featureless pattern of Sn K-edge XANES for supported Ir–Sn samples, the shoulder peak at 29 201 eV due to Sn(0) sites was almost buried beneath the pattern of Sn(IV) sites. In addition, the energy resolution at the Sn K-edge was greater (3–5 eV) compared to that at the Ir L_3-edge and the contribution from the minor component was difficult to detect in the broader spectra. In this sense, Sn K-edge EXAFS was more sensitive in detecting metallic Sn–Ir alloy as the interatomic pair peak in the Fourier transform (Fig. 6), rather than the overlapping, broad pattern in the Sn K-edge XANES (Fig. 4). The population of alloy seems to be greater in the case of MCM-41. The absence of a long distance Sn–O is consistent with the absence of SnO_2 nanoparticles.[47] No Cl surrounding the Sn, which was present in the precursor organometallic cluster, was evidenced for either sample. In summary, after reduction, the Cl contribution was completely removed by O neighbours and some of the Sn was alloyed with Ir in well-dispersed metal particles. No bulk tin oxide was formed.

For the dual source-derived catalyst, the fit results of the EXAFS data of the Ir L_3 edge showed that by increasing the Ir/Sn atomic ratio from 2 to 6, no relevant variation in the Ir surrounding, *i.e.* the N_{Ir-M} coordination number, was detectable (Tables 3 and 4).

Interesting is the presence of a second Sn–O scattering path at 0.28 Å for the fit of the EXAFS Sn K-edge data of $Ir_{1.8}$ + Sn/SiO_2, which may be consistent with the presence of bulk SnO_2,[47] and the lower coordination number for the path Sn–Ir. The fit result is consistent with a lower amount of Sn in the Ir particles and the presence of some bulk SnO_2.

After a catalysis run of 24 h, the average size of Ir nanoparticles over Ir/MCM-41 catalyst (1.8 nm) was about twice as large as on the fresh reduced catalyst (0.7 nm), while the $[Ir_4Sn_2]$/MCM-41 metal particles do not increase in size (0.9–1.1 nm; Fig. 7). For both samples after catalysis, the peak corresponding to the O surface atoms (0.18 nm, phase shift uncorrected) was significantly reduced, even in the case where the metal phase remained well dispersed. This fact strongly suggests that the Ir atoms previously in intimate contact with the support were covered by carbon residues due to the dehydrogenation of propane.

Table 4 EXAFS data fit at the Ir L_3-edge, for silica- and MCM-41-supported catalysts

	Shell Ir–O	Shell Ir–Ir and Ir–Sn	Shell Ir–Sn	D_{EXAFS} (Å)	$D_{HR\text{-}TEM}$
$[Ir_4Sn_2]/SiO_2$	—	$N = 6.5$ $\sigma = 0.079$ $R = 2.692$ $\Delta E_0 = -2.8$	—	14	11.8
$[Ir_4Sn_2]$/MCM-41	$N = 3.5$ $\sigma = 0.076$ $R = 2.000$ $\Delta E_0 = 14$	$N = 3.4$ $\sigma = 0.085$ $R = 2.597$ $\Delta E_0 = -10$	—	9	10.9
$[Ir_6Sn]$/MCM-41	$N = 4.9$ $\sigma = 0.10$ $R = 1.993$ $\Delta E_0 = 12.6$	$N = 3.1$ $\sigma = 0.081$ $R = 2.666$ $\Delta E_0 = 0.0$	—	8	11.5
$Ir_{1.8}$ + Sn/SiO_2	—	$N = 6.9$ $\sigma = 0.074$ $R = 2.702$ $\Delta E_0 = 0.0$	—	15	13.6
$Ir_{5.9}$ + Sn/SiO_2	$N = 1.8$ $\sigma = 0.078$ $R = 1.992$ $\Delta E_0 = 12.8$	$N = 6.9$ $\sigma = 0.078$ $R = 2.691$ $\Delta E_0 = 0.0$	—	15	17.9
Ir/MCM-41	$N = 4.9$ $\sigma = 0.10$ $R = 1.990$ $\Delta E_0 = 13.9$	$N = 2.8$ $\sigma = 0.071$ $R = 2.691$ $\Delta E_0 = 0.0$	—	7	11.9
Ir/MCM-41 after 24 h catalysis run	$N = 1.8$ $\sigma = 0.10$ $R = 1.973$ $\Delta E_0 = 11.7$	$N = 7.6$ $\sigma = 0.085$ $R = 2.680$ $\Delta E_0 = 0.3$	—	18	
$[Ir_4Sn_2]$/MCM-41 after 24 h catalysis run	$N = 2.8$ $\sigma = 0.10$ $R = 1.961$ $\Delta E_0 = 11.4$	$N = 4.7$ $\sigma = 0.091$ $R = 2.663$ $\Delta E_0 = 0.2$	—	11	10.8

The distance is expressed in angstroms, the DW factor in angstroms, and the energy shift in eV.

4. Discussion

In a previous paper[31] mainly focused on the catalytic behavior of Ir–Sn bimetallic catalysts, the catalytic performances were ascribed to geometrical effects, inhibiting the formation of adjacent-atom aggregates (responsible for hydrogenolysis), as well as to electronic effects, reducing the electronic density of the Ir sites, exerted by Sn atoms. Ir–Sn systems, obtained *via* the *single source* method, showed very high selectivity (95%) to propene at interesting values of propane conversion (18%) for the dehydrogenation of propane at 773 K and a high stability during the reaction time (negligible loss of activity and no agglomeration of the metallic particles).[31] However, neither the exact localization of Sn with respect to Ir sites nor the electronic effect of the Sn sites on the Ir ones (by evaluation of the oxidation states of Sn species) could be determined in that work. Such parameters are of great importance for making hypotheses on structure–activity relationships and, thus, for a rational design of nanostructures and, in particular, of effective and selective catalytic sites.

Upon impregnation and interaction with the support surface, the $(NEt_4)_2[Ir_4(CO)_{12}(SnCl_3)_2]$ cluster deposited onto MCM-41 did not change the metal frame nuclearity (similar coordination numbers at EXAFS Ir-edge and Sn-edge). The two Sn–Ir distances characteristic of the cluster cage structure are only slightly changed into one at longer R (2.847 Å). After reduction, the Cl contribution was completely removed by O neighbours and the Sn is alloyed with Ir in small metal particles. No bulk tin oxide was formed. The same happens also when starting from the Ir_6Sn cluster.

The Sn K-edge XANES data show that as the Sn amount in the cluster is decreased, the absorption edge shifts toward the higher energy side. This trend suggests that Sn acts as an effective electron donor to Ir and the donation extent per Sn atom is greater as the Sn amount became relatively smaller. The higher the total Sn amount, the higher is the overall electron-rich character of the Ir.

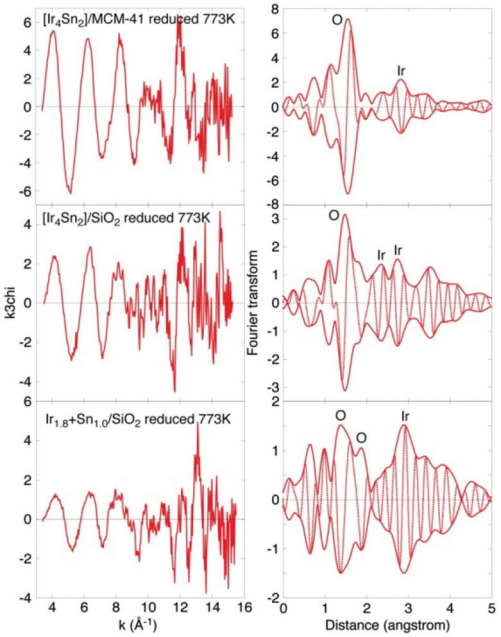

Fig. 6 Sn K-edge FFT EXAFS spectra of $[Ir_4Sn_2]$/MCM-41, $[Ir_4Sn_2]/SiO_2$ and $Ir_{1.8}$ + Sn/SiO_2 after reduction under H_2 flow.

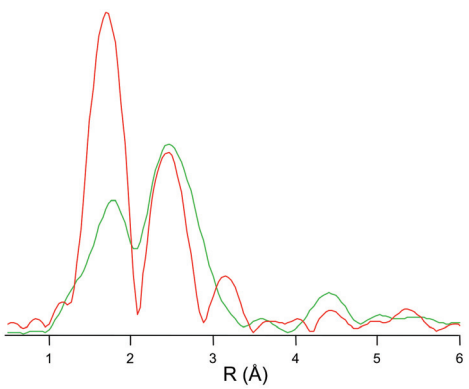

Fig. 7 Ir L_3-edge FFT EXAFS spectra (phase shift uncorrected) of $[Ir_4Sn_2]$/MCM-41 before (red) and after a 24 h catalysis run (green).

The morphology of the samples evolved in a different way upon reduction, depending on the sample preparation approach. In fact, by reducing the samples prepared depositing bimetallic clusters on silica (*single source*), small alloy metal particles with Sn interacting with surface O atoms are formed with an increase of the average metal cage size with respect to the starting cluster (metal coordination around Ir 6.5 *vs.* 3.5 corresponding to very small particles of about 30 atoms, consistent with an average particle diameter of 1.2 nm, as from HR-TEM data). Furthermore, the total Ir coordination around Sn decreases from 4 to 2, suggesting that only 50% of the Sn atoms are still alloyed with Ir, the remaining being atomically dispersed on the support surface (even though no evident presence of bulk tin oxide aggregates was detected by EDX analysis in the range of 5 nm scale[31]).

In contrast, by reduction of the samples prepared *via* the dual source approach supported on non-ordered silica, some SnO_x species were produced together with small alloyed Ir–Sn metal particles and a further increase of the average metal cage size was revealed based on the Sn and Ir EXAFS analyses.

The dual step system $Ir_{1.8}$ + Sn/SiO_2 after reduction shows metal particles with an average size of 1.4 nm (as from HR-TEM, and N = 6.9 at Ir-edge EXAFS), with an even lower fraction of tin alloyed with Ir (N = 0.6 at Sn-edge EXAFS) and the formation of some bulk tin oxide particles.

By varying the molar ratio of Ir/Sn, the metal particle size after reduction does not significantly change, as Ir-edge EXAFS and HR-TEM provide average diameters of 1.7–1.8 nm for the $Ir_{5.9}$ + Sn catalysts.

The Sn–Ir alloy seems to be the active phase for the selective dehydrogenation, most typically observed for $[Ir_4Sn_2]$/MCM-41 (Table 2; N(Sn–Ir) = 4.6 in total). The dominant oxidic Sn species, most typically observed for $Ir_{1.8}$ + Sn/SiO_2 (N_{Sn-O} = 6.5–6.6 in total), plays virtually no role in catalysis. The catalytic results of $Ir_{1.8}$ + Sn/SiO_2 were indeed similar to those of Ir/SiO_2. The curve fit results for $[Ir_4Sn_2]/SiO_2$ showed an intermediate situation between the two samples: a mixture of Ir–Sn alloy and Sn in the higher oxidation state. The extent of Ir–Sn alloy formation was correlated with the selective dehydrogenation catalysis.

In addition, the effect of Sn–Ir interaction on the MCM-41-supported catalysts structure is clearly visible in the following behaviour. After 24 hours of catalysis, the Ir catalyst underwent a consistent sintering effect (the final metal particle average size increased from 0.7 to 1.8 nm, which is more than twice as large as in the freshly reduced sample), with a corresponding decrease of the total amount of chemisorbed CO. In contrast, the $[Ir_4Sn_2]$-derived catalyst preserved intact its starting size (1.1 nm) and its linear CO components ratio and position: the CO chemisorption decrease was due to a partial metal surface coverage by carbonaceous residues, as suggested also by the Ir-edge EXAFS data and by C, H, N elemental analysis, showing a total carbon content of 2.42 wt%.

A structural model can be proposed (Scheme 2), where tin is present in two states: (i) as metallic tin, Sn(0), in bimetallic Ir–Sn nanoparticles; (ii) as oxidized phase, SnO_x, where x = 1–2, at the interface between the bimetallic Ir–Sn nanoparticles and the silica supports. The relative distribution of tin in the two phases (and oxidation states) strongly depends on the metal precursor, on the tin loading, and to a minor extent on the silica support.

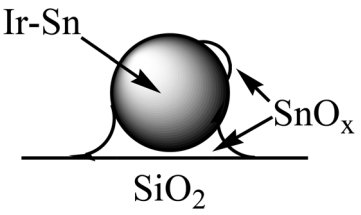

Scheme 2

The presence of a layer of SnO_x on the surface of metallic nanoparticles cannot be excluded, as it is reported for other bimetallic systems, like Ru–Sn.[13] At high Sn loadings, Sn could be also present as segregated SnO_x nanoparticles dispersed on the support.

On both samples, after catalysis, the peak corresponding to the O surface atoms largely decreased, even in the absence of a remarkable sintering of metal particles (N_{Ir-Ir} increased from 3.4 to 4.7 and particle mean diameter from 0.9 to 1.1 nm), which strongly suggests that some of the Ir atoms previously in strong contact with the support are now covered by carbon residues, as suggested also by the strong decrease of the overall integrated area of DRIFT spectra CO bands and confirmed by values of C, H, N elemental analysis spanning the range of 0.9–2.9 wt% of carbon.

5. Conclusions

Ir–Sn bimetallic particles, supported on silica with different morphologies, showed remarkable catalytic properties in the selective dehydrogenation of light alkanes. The surface Ir–Sn can be obtained *via* deposition of the molecular organometallic Ir–Sn clusters or *via* deposition of an Sn organometallic precursor onto pre-formed Ir metal particles.

From our data, a neat ensemble effect in the catalyst could not be established, since Sn–Ir and Ir–Ir interactions were not clearly distinguishable. However, a noteworthy Sn → Ir donation was shown by XANES measurements, suggesting at least a relevant electronic effect in the metallic particles. It is likely that a concurrent counterbalance of the two effects leads to the peculiar catalytic properties of these solids in the dehydrogenation reaction.

On the basis of the analytical techniques employed, some appreciable differences could be pointed out, depending on the nature of the precursors. The particles prepared from the molecular bimetallic clusters are more stable, both in dimensions and in composition: chlorides are immediately lost upon reduction, the Ir–Sn ratio showed small variations, and the

metal particle dimensions were relatively constant, even if much larger than the molecular dimensions of the starting clusters. In contrast, the particles prepared *via* the dual source approach showed the formation of tin oxide, corresponding to an increase of the Ir/Sn ratio in the alloy and a larger size. Thus, the presence of SnO_x species, decorating the Ir particles, does not hamper sintering of the noble metal. Finally, the Sn–Ir ratio in the precursor seems to be of little influence for the properties of the final supported metal particles.

Acknowledgements

The SOLEIL synchrotron light laboratory in Saclay (Paris, France) and the staff of the SAMBA beamline are gratefully acknowledged for the support and technical assistance. The X-ray absorption experiments were performed with the approval of the Photon Factory Proposal Review Committee (No. 2005G221) and the SPring-8 Program Review Committee (2004A0122-NXa300-np and 2003B0386-NXa-np). R.P., M.G. and V.D.S. thank the Italian Ministry of Education, University and Research through the Project "ItalNanoNet" (Rete Nazionale di Ricerca sulle Nanoscienze; Prot. No. RBPR05JH2P).

Notes and references

1 M. Flytzani-Stephanopoulos, B. Zugic, B. Ricks and G. Stephanopoulos, *PCT Int. Appl.*, WO 2010096812 A2 20100826, 2010.
2 A. Corma, S. Iborra and A. Velty, *Chem. Rev.*, 2007, **107**, 2411.
3 E. L. Kunkes, D. A. Simonetti, R. M. West, J. C. Serrano-Ruiz, C. A. Gartner and J. A. Dumesic, *Science*, 2008, **322**, 417.
4 K. Weissermel and H. J. Arpe, *Industrial organic chemistry*, Wiley-VCH, Weinheim, Germany, 2003, p. 64.
5 J. M. Thomas, B. F. G. Johnson, R. Raja, G. Sankar and P. A. Midgley, *Acc. Chem. Res.*, 2003, **36**, 20.
6 S. Recchia, C. Dossi, N. Poli, A. Fusi, L. Sordelli and R. Psaro, *J. Catal.*, 1999, **184**, 1.
7 A. Siani, B. Captain, O. S. Alexeev, E. Stafyla, A. B. Hungria, P. A. Midgley, J. M. Thomas, R. D. Adams and M. A. Amidiris, *Langmuir*, 2006, **22**, 5160.
8 V. Dal Santo, A. Gallo, A. Naldoni, M. Guidotti and R. Psaro, *Catal. Today*, 2012, **197**, 190.
9 D. E. Resasco and G. L. Haller, *Catalysis*, Royal Society Chemistry, Cambridge, UK, 1994, vol. 11, p. 379.
10 O. A. Barias, A. Holmen and E. A. Blekkan, *J. Catal.*, 1996, **158**, 1.
11 J. C. Moreno-Pirajan, V. S. Garcia-Cuello and L. Girald, *Top. Catal.*, 2011, **54**, 146.
12 A. Gallo, T. Montini, M. Marelli, A. Minguzzi, V. Gombac, R. Psaro, P. Fornasiero and V. Dal Santo, *ChemSusChem*, 2012, **5**, 1800.
13 A. Gallo, C. Pirovano, M. Marelli, R. Psaro and V. Dal Santo, *Chem. Vap. Deposition*, 2011, **16**, 305.
14 J. H. Sinfelt, *Science*, 1977, **195**, 641.
15 B. Chen and J. G. Goodwin, *J. Catal.*, 1996, **158**, 228.
16 J. J. Dalmon and G. A. Martin, *J. Catal.*, 1980, **66**, 214.
17 V. Ponec and W. H. Sachtler, *J. Catal.*, 1972, **24**, 250.
18 Y. H. Romdhane, B. Bellamy, V. De Gouvela and A. Masson, *Appl. Surf. Sci.*, 1988, **31**, 383.
19 G. Leclercq, L. Leclercq and R. Maurel, *J. Catal.*, 1977, **50**, 87.
20 P. G. Menon and Z. Paal, *Ind. Eng. Chem. Res.*, 1997, **36**, 3282.
21 A. Virnovskaia, S. Morandi, E. Rytter, G. Ghiotti and U. Olsbye, *J. Phys. Chem. C*, 2007, **111**, 14732.
22 C. Yu, Q. Ge, H. Xu and W. Li, *Ind. Eng. Chem. Res.*, 2007, **46**, 8722.
23 M. J. Height, S. E. Pratsinis, O. Mekasuwandunrong and P. Praserthdam, *Appl. Catal. B: Environ.*, 2006, **63**, 305.
24 R. Strobel, W. J. Stark, L. Madler, S. E. Pratsinis and A. Baiker, *J. Catal.*, 2003, **213**, 296.
25 F. Humblot, J. P. Candy, F. Le Peltier, B. Didillon and J. M. Basset, *J. Catal.*, 1998, **179**, 459.
26 C. Yu, Q. Ge, H. Xu and W. Li, *Appl. Catal. A: Gen.*, 2006, **315**, 58.
27 Q. Li, Z. Sui, X. Zhou, Y. Zhu, J. Zhou and D. Chen, *Top. Catal.*, 2011, **54**, 888.
28 F. B. Passos, M. Schmal and M. A. Vannice, *J. Catal.*, 1996, **160**, 106.
29 G. F. Santori, M. L. Casella and O. A. Ferretti, *J. Mol. Catal. A: Gen.*, 2002, **186**, 223.
30 D. M. Sommerville and J. R. Shapley, *Catal. Lett.*, 1998, **52**, 123.
31 M. Guidotti, V. Dal Santo, A. Gallo, E. Gianotti, G. Peli, R. Psaro and L. Sordelli, *Catal. Lett.*, 2006, **112**, 89.
32 C. T. Kresge, M. E. Leonowicz, W. J. Roth, J. C. Vartuli and J. S. Beck, *Nature*, 1992, **359**, 710.
33 L. Garlaschelli, F. Greco, G. Peli, M. Manassero, M. Sansoni and R. Della Pergola, *Dalton Trans.*, 2003, 4700.
34 V. Dal Santo, C. Dossi, A. Fusi, R. Psaro, C. Mondelli and S. Recchia, *Talanta*, 2005, **66**, 674.
35 L. Ankudinov, B. Ravel, J. J. Rehr and S. D. Condradson, *Phys. Rev. B: Condens. Matter*, 1998, **58**, 7665.
36 M. R. Churchill and J. P. Hutchinson, *Inorg. Chem.*, 1978, **17**, 3528.
37 L. Garlaschelli, S. Martinengo, P. L. Bellon, F. Demartin, M. Manassero, M. Y. Chiang, C. Y. Wei and R. Bau, *J. Am. Chem. Soc.*, 1984, **106**, 6664.
38 L. Garlaschelli, F. Greco, G. Peli, M. Manassero, M. Sansoni and R. Della Pergola, *Dalton Trans.*, 2003, 4700.
39 M. Frank, R. Kuhnemuth, M. Baumer and H. J. Freund, *Surf. Sci.*, 2000, **454–456**, 968.
40 A. Erdőhely, K. Fodor and G. Suru, *Appl. Catal. A: Gen.*, 1996, **139**, 131.
41 F. J. C. M. Toolenaar, A. G. T. M. Bastein and V. Ponec, *J. Catal.*, 1983, **82**, 35.
42 F. Solymosi, É. Novák and A. Molnár, *J. Phys. Chem.*, 1990, **94**, 7250.

43 K. Tanaka, K. L. Watters and R. F. Howe, *J. Catal.*, 1982, **75**, 23.
44 G. B. McVicker, R. L. Baker, R. L. Garten and E. L. Kugler, *J. Catal.*, 1980, **65**, 207.
45 M. Guisnet, Modes of coke formation and deactivation, in *Deactivation and Regeneration of Zeolite Catalysts*, ed. M. Guisnet and F. Ramoa Ribeiro, Imperial College Press, 2011, pp. 115–138.
46 L. Garlaschelli, R. Della Pergola and S. Martinengo, *Inorg. Synth.*, 1991, **28**, 245.
47 S. R. Davis, A. V. Chadwick and J. D. Wright, *J. Phys. Chem. B*, 1997, **101**, 9901.

